

Adsorption-Controlled Growth of Ga₂O₃ by Suboxide Molecular-Beam Epitaxy

Patrick Vogt,^{1, a)} Felix V. E. Hensling,¹ Kathy Azizie,¹ Celesta S. Chang,² David Turner,^{3, 4} Jisung Park,¹ Jonathan P. McCandless,⁵ Hanjong Paik,^{1, 6} Brandon J. Bocklund,⁷ Georg Hoffman,⁸ Oliver Bierwagen,⁸ Debdeep Jena,^{1, 5, 9} Huili G. Xing,^{1, 5, 9} Shin Mou,³ David A. Muller,^{2, 9} Shun-Li Shang,⁷ Zi-Kui Liu,⁷ and Darrell G. Schlom^{1, 9, 10, b)}

¹⁾*Department of Materials Science and Engineering, Cornell University, Ithaca, New York 14853,*

USA

²⁾*School of Applied and Engineering Physics, Cornell University, Ithaca, New York 14853,*

USA

³⁾*Air Force Research Laboratory, Materials and Manufacturing Directorate, Wright Patterson AFB, Ohio 45433,*

USA

⁴⁾*Azimuth Corporation, 2970 Presidential Drive, Suite 200, Fairborn, Ohio 45324,*

USA

⁵⁾*School of Electrical and Computer Engineering, Cornell University, Ithaca, New York 14853,*

USA

⁶⁾*Platform for the Accelerated Realization, Analysis and Discovery of Interface Materials (PARADIM), Cornell University, Ithaca, New York 14853, USA*

⁷⁾*Department of Materials Science and Engineering, Pennsylvania State University, University Park, Pennsylvania 16802,*

USA

⁸⁾*Paul-Drude-Institut für Festkörperelektronik, Leibniz-Institut im Forschungsverbund Berlin e.V., Hausvogteiplatz 5–7,*

10117 Berlin, Germany

⁹⁾*Kavli Institute at Cornell for Nanoscale Science, Ithaca, New York 14853, USA*

¹⁰⁾*Leibniz-Institut für Kristallsüchtung, Max-Born-Str. 2, 12489 Berlin, Germany*

This paper introduces a growth method—suboxide molecular-beam epitaxy (*S*-MBE)—which enables the growth of Ga₂O₃ and related materials at growth rates exceeding 1 μm hr⁻¹ with excellent crystallinity in an adsorption-controlled regime. Using a Ga + Ga₂O₃ mixture with an oxygen mole fraction of $x(\text{O}) = 0.4$ as an MBE source, we overcome kinetic limits that had previously hampered the adsorption-controlled growth of Ga₂O₃ by MBE. We present growth rates up to 1.6 μm hr⁻¹ for Ga₂O₃/Al₂O₃ heterostructures with unprecedented crystalline quality and also at unparalleled low growth temperature for this level of perfection. We combine thermodynamic knowledge of how to create molecular-beams of targeted suboxides with a kinetic model developed for the *S*-MBE of III-VI compounds to identify appropriate growth conditions. Using *S*-MBE we demonstrate the growth of phase-pure, smooth, and high-purity homoepitaxial Ga₂O₃ films that are thicker than 4 μm. With the high growth rate of *S*-MBE we anticipate a significant improvement to vertical Ga₂O₃-based devices. We describe and demonstrate how this growth method can be applied to a wide-range of oxides. *S*-MBE rivals leading synthesis methods currently used for the production of Ga₂O₃-based devices.

I. INTRODUCTION

Molecular-beam epitaxy (MBE) involves the growth of epitaxial thin films from molecular-beams. In ‘conventional’ MBE the molecular-beams consist of elements. An example is the Ga (*g*) species that evaporate from a heated crucible containing Ga (*l*) or the As₄ (*g*) species that evaporate from a heated crucible containing As (*s*), where *g*, *l*, and *s* denote gaseous, liquid, and solid, respec-

tively. In gas-source MBE the species in the molecular-beams originate from gases that are plumbed into the MBE from individual gas cylinders, for example, arsine or phosphine. In metal-organic MBE the species in the molecular-beams are metal-organic molecules like trimethylgallium or trimethylaluminum.¹ ‘Suboxide MBE’ refers to an MBE growth process utilizing molecular-beams of suboxides like Ga₂O (*g*) or In₂O (*g*). We have applied this method to the growth of Ga₂O₃ thin films and find that it can produce epitaxial Ga₂O₃ films with far greater perfection and at much higher growth rates than currently demonstrated by other MBE methods for the growth of this material.

^{a)}Electronic mail: pv269@cornell.edu

^{b)}Electronic mail: schlom@cornell.edu

A. ‘Conventional’ MBE of Ga₂O₃ and related materials

Gallium-sesquioxide (Ga₂O₃) synthesized in its different polymorphs [i.e., α-Ga₂O₃ (rhombohedral), β-Ga₂O₃ (monoclinic), γ-Ga₂O₃ (cubic spinel), ε-Ga₂O₃ (hexagonal), and κ-Ga₂O₃ (orthorhombic)], is an emerging semiconductor possessing promising features for unprecedented high-power electronics. This is due to its large band gap (~ 5 eV)^{2,3} and very high breakdown field (up to 8 MV cm⁻¹).⁴ The band gap of Ga₂O₃ may be widened by alloying Ga₂O₃ with Al₂O₃ to form (Al_xGa_{1-x})₂O₃.³ The synthesis of (Al_xGa_{1-x})₂O₃/Ga₂O₃ heterostructures with high Al content x is desired for high-power transistors with large band gap offsets.^{3,5,6}

It is known that the ‘conventional’ MBE of Ga₂O₃—i.e., when supplying monoatomic Ga and active O species during growth—is strongly limited by the formation and subsequent desorption of its volatile suboxide Ga₂O.⁷⁻¹¹ In the adsorption-controlled regime (i.e., grown with an excess of Ga), its growth rate strongly decreases with increasing Ga flux, ϕ_{Ga} , because not enough oxygen is available to oxidize the physisorbed Ga₂O to Ga₂O₃ (s) and the Ga₂O desorbs from the hot substrate. At sufficiently high ϕ_{Ga} , film growth stops, and even goes negative (i.e., the Ga₂O₃ film is etched).⁸ This effect is enhanced as the growth temperature, T_G , increases due to the thermally activated desorption of Ga₂O from the growth surface. The enhanced, T_G -induced Ga₂O desorption leads to a decreasing growth rate even in the O-rich regime, resulting in a short growth rate plateau (the value of which is far below the available active O flux¹²), followed by an even further decreasing growth rate in the adsorption-controlled regime.^{9,12,13} These effects, i.e., the O-deficiency induced and thermally activated desorption of suboxides,^{9,11-13} are detrimental for the growth of III-VI (e.g., Ga₂O₃) and IV-VI materials in the adsorption-controlled regime.

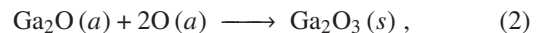
Nevertheless, the MBE of thin films in the adsorption-controlled growth regime is often desired for high crystal perfection,¹⁴⁻¹⁶ smooth surface morphology,¹⁷ avoiding undesired oxidation states,^{18,19} or suppressing the formation of electrically compensating defects.^{20,21}

The decreasing growth rate of Ga₂O₃ is microscopically explained by a complex two-step reaction mechanism.^{11,12} In the *first* reaction step, all Ga oxidizes

to Ga₂O via the reaction



with adsorbate and gaseous phases denoted as a and g , respectively. The Ga₂O formed may either desorb from the growth surface (in the O-deficient regime or at elevated T_G) or be further oxidized to Ga₂O₃ via a *second* reaction step through the reaction



with the solid phase denoted as s .

This two-step reaction mechanism and the resulting Ga₂O desorption defines the growth rate-limiting step for the ‘conventional’ MBE of Ga₂O₃ and related materials.^{11,12} This results in a rather narrow growth window associated with low growth rates in the adsorption-controlled regime.^{7-9,11} A similar growth rate-limiting behavior, based on this two-step reaction mechanism, has also been reported for the growth of other III-VI (e.g., In₂O₃) and IV-VI (e.g., SnO₂) compounds by ‘conventional’ MBE.^{8,11,13} This two-step growth process for the growth of III-VI and IV-VI oxides by ‘conventional’ MBE is fundamentally different from the single-step reaction mechanism of, for example, III-V²²⁻²⁴ and II-VI²⁵ compounds. It can be attributed to the different electronic configurations of the compound constituents, resulting in different compound stoichiometries between III-VI and IV-VI compared with III-V and II-VI materials, respectively.

In the growth method introduced in this work, which we call *suboxide* MBE (*S*-MBE), we avoid the first reaction step (1) by directly supplying a Ga₂O (g) molecular-beam to the growth front on the substrate surface. Using this approach, we bypass the growth rate-limiting step for ‘conventional’ Ga₂O₃ MBE by removing the O-consuming step to Ga₂O formation that occurs on the substrate in the ‘conventional’ MBE growth of Ga₂O₃.^{11,12} A related approach has been used by Ghose *et al.*^{26,27} with Ga₂O provided from Ga₂O₃ source material heated to temperatures well in excess of 1600 °C to produce a molecular beam of Ga₂O for the growth of Ga₂O₃ films by MBE.²⁸ Motivated by known vapor pressure data of oxides²⁹ and their mixtures with the respective metals, e.g., Ga + Ga₂O₃,³⁰ as well as the possibility of decomposing Ga₂O₃ by Ga and SnO₂ by Sn under MBE conditions,⁸ Hoffmann *et al.*³¹ have demonstrated how mixtures of Ga with Ga₂O₃ and Sn with SnO₂ provide MBE-relevant fluxes of Ga₂O and SnO, respectively, at source

temperatures below 1000 °C. This prior work has grown films using suboxide molecular beams by MBE at growth rates $< 0.2 \mu\text{m hr}^{-1}$.^{31,32}

As we demonstrate, *S*-MBE enables the synthesis of Ga_2O_3 in the highly adsorption-controlled regime, at growth rates $> 1 \mu\text{m hr}^{-1}$ with unparalleled crystalline quality for $\text{Ga}_2\text{O}_3/\text{Al}_2\text{O}_3$ heterostructures as well as homoepitaxial Ga_2O_3 at relatively low T_G . The growth rate of *S*-MBE is competitive with other established growth methods used in semiconductor industry—such as chemical vapor deposition (CVD)³³ or metal-organic CVD (MOCVD)³⁴—and moreover, leads to better structural perfection of the obtained thin films. With this improved perfection we expect an improvement of *n*-type donor mobilities in Ga_2O_3 thin films doped with Sn, Ge, or Si grown by *S*-MBE, as well. The relatively low T_G at which it becomes possible to grow high-quality films by *S*-MBE is a crucial enabler for materials integration where temperatures are limited, e.g., back end of line (BEOL) processes.

Figure 1 illustrates a schematic of how growth rate depends on cation flux during the MBE growth of different types of compounds, where both axes are normalized by the anion flux. Figure 1(a) depicts the observed behavior for III-V compounds, e.g., GaN.²⁴ Figure 1(b) shows the observed behavior for III-VI compounds, e.g., Ga_2O_3 , when the group III cation is supplied by a molecular-beam of the group III element (e.g., Ga).⁸ In Fig. 1(c), the anticipated behavior for III-VI compounds is plotted, e.g., Ga_2O_3 , when the group III element is supplied by a molecular-beam of a III₂VI subcompound containing the group III constituent (e.g., Ga_2O).¹² The units of the horizontal and vertical axes are chosen to make the crossover occur at values of unity. For the sake of simplicity, henceforth, we only discuss the reaction behavior of GaN and Ga_2O_3 in detail. We emphasize, however, this discussion holds true for the MBE growth of AlN,²² InN,²³ In_2O_3 (Refs. 8,11,13) and other III-VI,^{11,35} and II-VI compounds.²⁵

As drawn in Figs. 1(a)–1(c), the growth rate of GaN and Ga_2O_3 increases linearly with increasing ϕ_{Ga} in the N-rich [Fig. 1(a)] and O-rich regimes [Fig. 1(b) and 1(c)], respectively. Here, the incorporation of Ga is limited by the impinging ϕ_{Ga} or Ga_2O flux, $\phi_{\text{Ga}_2\text{O}}$ (i.e., Ga-transport and Ga_2O -transport limited growth regimes).

For GaN MBE [Fig. 1(a)], once the supplied ϕ_{Ga} exceeds the flux ϕ_{N} of active available N, the growth rate saturates, is independent of the $\phi_{\text{Ga}}/\phi_{\text{N}}$ ratio, and is limited by

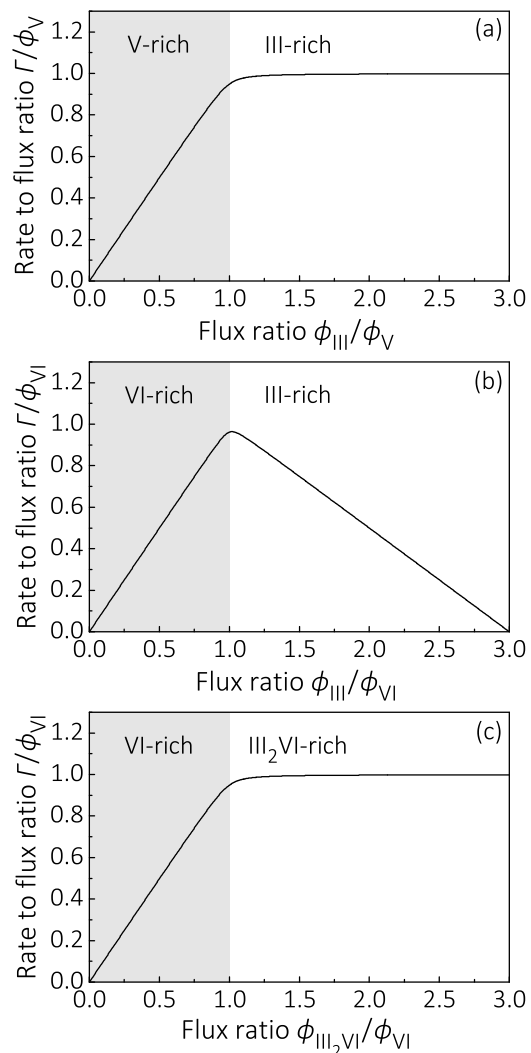


FIG. 1. (a) and (b) Schematic growth rate as observed for III-V (e.g., GaN)²⁴ and III-VI compounds (e.g., Ga_2O_3)¹¹ as a function of the III/V (e.g., $\phi_{\text{Ga}}/\phi_{\text{N}}$) and III/VI flux ratios (e.g., $\phi_{\text{Ga}}/\phi_{\text{O}}$), respectively. (c) Anticipated growth rate behavior of III-VI compounds (e.g., Ga_2O_3)¹² as a function of the III₂VI/VI flux ratio (e.g., $\phi_{\text{Ga}_2\text{O}}/\phi_{\text{O}}$). All schematic growth rate evolutions are normalized by the respective fluxes of active available group V (ϕ_{V}) and group VI elements (ϕ_{VI}). Each plot is at a constant T_G . Anion-rich and cation-rich regimes are indicated in gray and white, respectively.

ϕ_{N} and T_G . The measured plateau in growth rate for GaN MBE in the Ga-rich regime results from its single-step reaction kinetics. Here, Ga reacts directly with activated N via the reaction²⁴



and excess Ga either adsorbs onto or desorbs from the growth surface depending upon ϕ_{N} and T_G .

Figure 1(b) depicts the reaction kinetics of Ga_2O_3 in the Ga-rich regime (O-deficient growth regime) by supplying ϕ_{Ga} . Here, the growth rate linearly *decreases* with increasing ϕ_{Ga} , and the growth eventually stops at $\phi_{\text{Ga}} \geq 3\phi_{\text{O}}$ (in growth rate units). The fact that desorbing Ga_2O removes Ga *and* O from the growth surface—that cannot contribute to Ga_2O_3 formation—leads to the decreasing growth rate in the O-deficient growth regime.^{8,9,11} This behavior is microscopically governed by the two-step reaction process, Eqs. (1) and (2),¹¹ and is fundamentally different from the single-step reaction kinetics, Eq. (3), governing the MBE of GaN [Fig. 1(a)].

In Fig. 1(c), the anticipated growth kinetics of Ga_2O_3 while using a Ga_2O beam is depicted, showing a constant growth rate in the Ga_2O -rich regime (i.e., in an excess of Ga_2O).¹² Excess Ga_2O (that cannot be oxidized to Ga_2O_3) either accumulates or desorbs off the growth surface *without* consuming or removing active O from its adsorbate reservoir—similar to the case presented for GaN in Fig. 1(a). Thus, with *S*-MBE, one may effectively achieve single-step reaction kinetics for Ga_2O_3 MBE [reaction (2)], as is the case for the growth of GaN by MBE [reaction (3)].

The synthesis of III-V and II-VI materials with cation flux-independent growth rates in adsorption-controlled growth regimes—originating from their simple single-step reaction kinetics [e.g., reaction (3)]—is beneficial for device-relevant growth rate control and the improvement of their crystal properties.^{36–38} Through the use of *S*-MBE, we convert the complex two-step reaction kinetics of III-VI [e.g., reactions (1) and (2)] and IV-VI compounds into simple single-step kinetics [e.g., (2)], the same as observed for III-V and II-VI materials. We therefore expect a similar growth behavior during *S*-MBE, i.e., constant growth rates in the adsorption-controlled regime, which are highly scalable by the provided active O flux. Such a regime should allow III-VI thin films (e.g., Ga_2O_3) and IV-VI films (e.g., SnO_2) to be grown much faster with excellent crystal quality at relatively low T_G .

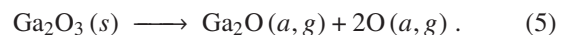
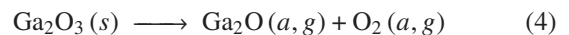
S-MBE utilizes molecular-beams of suboxides and builds upon prior thermodynamic work and thin film growth studies. For example, molecular-beams of the following suboxides have all been used in MBE: Ga_2O ,^{26,27,32} GdO ,^{39,40} LuO ,⁴⁰ LaO ,⁴⁰ NdO ,⁴¹ PrO ,^{42,43} ScO ,⁴⁴ SnO ,^{18,19,31,45,46} YO .³⁹ Even before these MBE studies, thin films of the suboxides SiO ,^{47,48} SnO ,^{49–53} and GeO ⁵⁴ had been deposited by thermal evaporation, exploiting the same underlying vapor

pressure characteristics that make *S*-MBE possible. In some of these cases the dominant species in the gas phase were not identified, but subsequent vapor pressure studies and thermodynamic calculations establish that they were suboxides.^{29,55}

What is new about *S*-MBE is the use of suboxide molecular-beams in a targeted way to achieve epitaxial growth of desired oxides (e.g., Ga_2O_3) at high growth rates in an adsorption-controlled regime. This enables the benefits of the far simpler (from a growth kinetics, growth control, and growth standpoint) plateau growth regime shown in Fig. 1(c) to be harnessed rather than the growth regime shown in Fig. 1(b) that has posed limits to the growth of Ga_2O_3 films by ‘conventional’ MBE up to now.

II. DETAILED DESCRIPTION OF *S*-MBE

The use of a Ga_2O (*g*) molecular-beam to grow Ga_2O_3 (*s*) thin films by MBE in the O-rich regime (i.e., in an excess of active O) has been demonstrated by placing the stoichiometric solid of the compound Ga_2O_3 into a crucible and using it as an MBE source.^{26,27} Possible reactions that produce a Ga_2O molecular-beam by the thermal decomposition of Ga_2O_3 are:

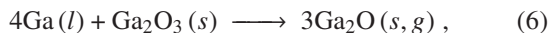


One disadvantage of using Ga_2O_3 (*s*) as the MBE source is that Ga_2O_3 does not evaporate congruently. Our thermodynamic calculations indicate that when Ga_2O_3 (*s*) is heated to a temperature where the Ga_2O (*g*) that it evolves has a vapor pressure of 0.1 Pa (a vapor pressure typical for MBE growth), that the Ga_2O molecular-beam is only 98.0% Ga_2O molecules. The other 2% of the beam is Ga, O_2 , and O species.

The other disadvantage of using Ga_2O_3 (*s*) as the MBE source is that quite high effusion cell temperatures are required to evolve appreciable $\phi_{\text{Ga}_2\text{O}}$; temperatures in excess of $\sim 1600^\circ\text{C}$,²⁸ $\sim 1700^\circ\text{C}$,⁵⁶ or $\sim 1800^\circ\text{C}$ ²⁶ have been used. At such high effusion cell temperatures, crucible choices become limited and prior researchers have used iridium crucibles.^{26,27,32,56} Ga_2O_3 thin films synthesized utilizing an iridium crucible at an effusion cell temperature of $\sim 1700^\circ\text{C}$ ⁵⁶ were limited to growth rates $< 0.14 \mu\text{m hr}^{-1}$ (Ref. 32) with $\sim 5 \times 10^{18} \text{ cm}^{-3}$ iridium contamination in the

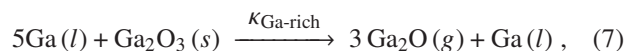
grown Ga_2O_3 films.^{56,57} These aspects of Ga_2O_3 compound sources hamper the synthesis of semiconducting Ga_2O_3 layers at growth rates exceeding $1 \mu\text{m hr}^{-1}$ with device-relevant material properties. For comparison, the $\text{Ga} + \text{Ga}_2\text{O}_3$ mixture that we describe next and have used to grow Ga_2O_3 films at growth rates exceeding $1 \mu\text{m hr}^{-1}$ provides a Ga_2O molecular-beam that is 99.98% pure according to our thermodynamic calculations. This is for the same Ga_2O vapor pressure of 0.1 Pa, which happens at a source temperature about 600°C lower for this $\text{Ga} + \text{Ga}_2\text{O}_3$ mixture than for pure Ga_2O_3 , enabling us to use crucibles that do not result in iridium-contaminated films.

Years ago as well as more recently, $\text{Ga} + \text{Ga}_2\text{O}_3$ -mixed sources producing a Ga_2O molecular-beam have been studied^{30,31} and suggested as efficient suboxide sources for oxide MBE.^{31,55} Using this mixed source, a Ga_2O (g) molecular-beam is produced by the chemical reaction

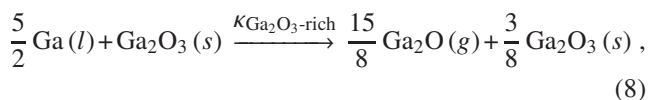


with the liquid phase denoted as l . S -MBE uses the thermodynamic³⁰ and kinetic⁸ properties of $\text{Ga} + \text{Ga}_2\text{O}_3$ mixtures favoring reaction (6) under MBE conditions.

For the S -MBE of Ga_2O_3 , we explored Ga -rich and Ga_2O_3 -rich mixtures of $\text{Ga} + \text{Ga}_2\text{O}_3$ with stoichiometries



and



respectively. The latter mixture has an oxygen mole fraction of $x(\text{O}) = 0.4$ and the properties of this Ga_2O_3 -rich mixture are described below. The corresponding reaction rate constants $\kappa_{\text{Ga-rich}}$ and $\kappa_{\text{Ga}_2\text{O}_3\text{-rich}}$ define the production rate of Ga_2O (g) at a given temperature T_{mix} of the $\text{Ga} + \text{Ga}_2\text{O}_3$ mixture.

The flux of Ga_2O (g) in the molecular-beam emanating from the mixed $\text{Ga} + \text{Ga}_2\text{O}_3$ sources is significantly larger than that of Ga (g)^{30,58} emanating from the same source. This is also true under MBE conditions.^{31,55} The resulting high ratio of $\text{Ga}_2\text{O}/\text{Ga} \gg 1$ provides a more controllable and cleaner growth environment than accessible by decomposing a stoichiometric Ga_2O_3 source, which produces molecular-beam ratios of $\text{Ga}_2\text{O}/\text{Ga}$, $\text{Ga}_2\text{O}/\text{O}_2$, and $\text{Ga}_2\text{O}/\text{O}$. Hence, the growth surface of the substrate during film growth using

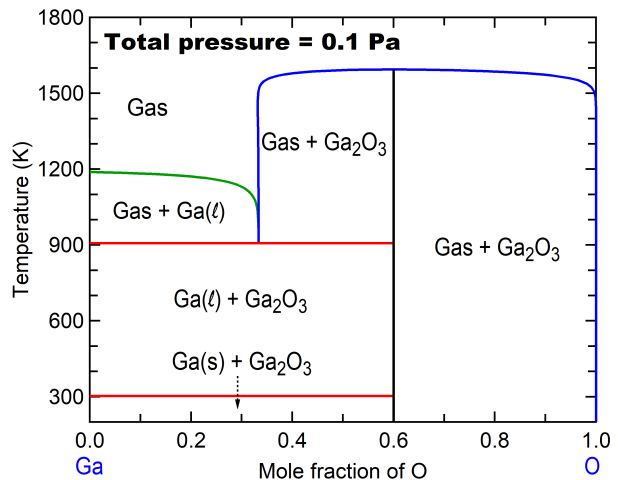


FIG. 2. Ga-O temperature-composition phase diagram under constant pressure $P = 0.1$ Pa. This phase diagram has been calculated at higher pressures by Ref. 59.

S -MBE is exposed to controllable and independently supplied molecular-beams of Ga_2O and reactive O adsorbates.

We have experienced that a Ga_2O_3 -rich mixture enables higher T_{mix} and higher, stable Ga_2O (g) molecular-beams than a Ga -rich mixture. This enables S -MBE to achieve higher growth rates. This experimental observation is confirmed by our thermodynamic calculations of the phase diagram of $\text{Ga}(l) + \text{Ga}_2\text{O}_3(s)$ mixtures, which we describe next.

The calculated Ga-O phase diagram in Fig. 2 shows that at T_{mix} below the three-phase equilibrium of gas + $\text{Ga}(l) + \text{Ga}_2\text{O}_3(s)$ around 907 K, a two-phase region of $\text{Ga}(l) + \text{Ga}_2\text{O}_3(s)$ forms, which does not change with respect to temperature or oxygen mole fraction between 0 and 0.6. Note that all thermodynamic calculations in the present work were performed using the Scientific Group Thermodata Europe (SGTE) substance database (SSUB5)⁶⁰ within the Thermo-Calc software.⁶¹ For $T_{\text{mix}} > 907$ K, the two-phase regions are gas + $\text{Ga}(l)$ when the mole fraction of oxygen is below 1/3, corresponding to what we refer to as Ga -rich mixtures, and gas + $\text{Ga}_2\text{O}_3(s)$ when the mole fraction of oxygen is between 1/3 and 0.6, which we refer to as Ga_2O_3 -rich mixtures. These two-phase regions become a single gas-phase region at T_{mix} of (907 – 1189) K for Ga -rich mixtures and at (907 – 1594) K for Ga_2O_3 -rich mixtures, respectively. All of these phase transition temperatures decrease with decreasing pressure⁵⁹ as shown on the pressure versus temperature ($P - T$) phase diagrams in Fig. 3.

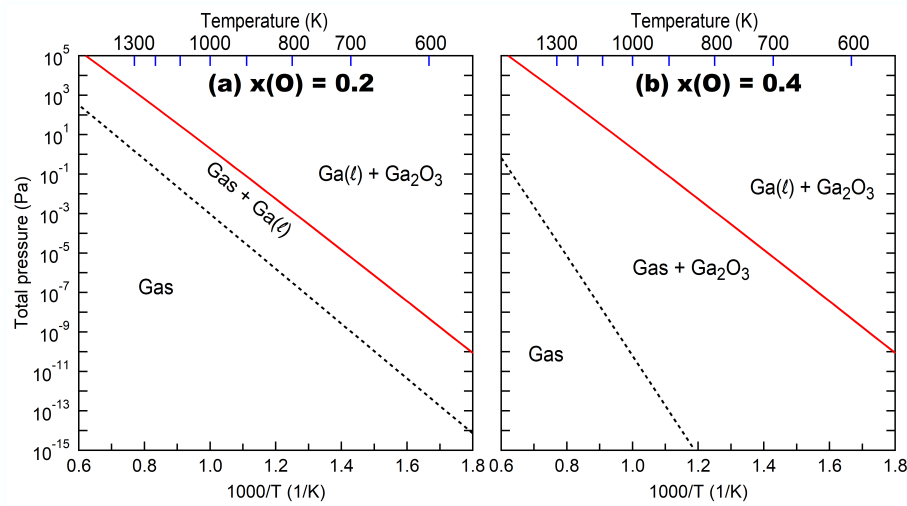


FIG. 3. Ga–O pressure versus temperature (P – T) phase diagrams at fixed mole fractions of oxygen of $x(\text{O}) = 0.2$ [panel (a)] and $x(\text{O}) = 0.4$ [panel (b)]. These oxygen mole fractions are chosen to illustrate the difference between (a) Ga-rich mixtures and (b) Ga_2O_3 -rich mixtures.

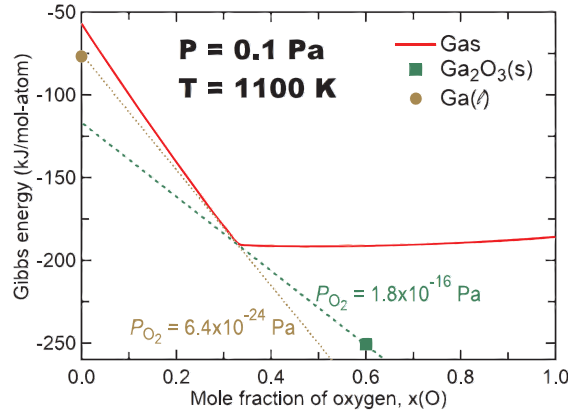


FIG. 4. Gibbs energies of the gas, $\text{Ga}(l)$, $\text{Ga}_2\text{O}_3(s)$ phases at temperature $T = 1100$ K and total pressure $P = 0.1$ Pa. The brown dotted line shows the activity (or partial pressure) of oxygen when $0 < x(\text{O}) < 0.33$. In this range the gas phase is in equilibrium with $\text{Ga}(l)$ and the activity of oxygen is 6.4×10^{-24} Pa. The green dashed line corresponds to the case where $0.33 < x(\text{O}) < 0.6$. In this range the gas phase is in equilibrium with $\text{Ga}_2\text{O}_3(s)$ and the activity of oxygen is $P_{\text{O}_2} = 1.8 \times 10^{-16}$ Pa. This difference in the partial pressure of O_2 between the two regimes is huge and shows the advantage of growing Ga_2O_3 films from Ga_2O_3 -rich ($\text{Ga} + \text{Ga}_2\text{O}_3$) mixtures.

To contrast the difference between Ga-rich versus Ga_2O_3 -rich mixtures we have performed additional thermodynamic calculations at oxygen mole fractions of $x(\text{O}) = 0.2$ and $x(\text{O}) = 0.4$. These two chosen oxygen mole fractions correspond to Ga-rich and Ga_2O_3 -rich mixtures, respectively. In Figs. 3(a) and 3(b) the solid (red) lines denote the three-phase equilibrium between gas + $\text{Ga}(l)$ + $\text{Ga}_2\text{O}_3(s)$; these are identical at $x(\text{O}) = 0.2$ and $x(\text{O}) = 0.4$. The dotted (black) lines denote the equilibrium between the gas and gas + $\text{Ga}(l)$ phase regions for $x(\text{O}) = 0.2$ and the gas and gas + $\text{Ga}_2\text{O}_3(s)$

phase regions for $x(\text{O}) = 0.4$, i.e., their respective boiling temperature/pressure.

Figure 4 shows Gibbs energies of the gas, $\text{Ga}(l)$, $\text{Ga}_2\text{O}_3(s)$ phases at temperature $T = 1100$ K and total pressure $P = 0.1$ Pa. There are seven distinct atomic and molecular species in the gas phase: Ga, Ga_2 , GaO , Ga_2O , O, O_2 , and O_3 . The kink in the Gibbs energy of the gas phase at $x(\text{O}) = 0.33$ corresponds to the composition of the Ga_2O species because it is the major species in the gas phase. It can be seen that the values of the oxygen activity in the gas + $\text{Ga}(l)$

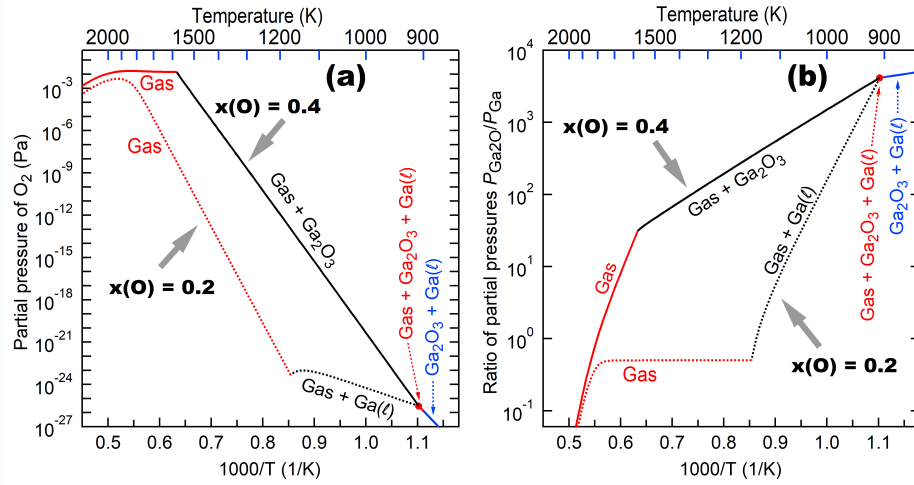


FIG. 5. (a) Partial pressure of oxygen and (b) ratio of the partial pressure of Ga_2O to that of Ga plotted as a function of temperature with the total pressure being 0.1 Pa for the mole fractions of oxygen at $x(O) = 0.2$ (dotted lines) and $x(O) = 0.4$ (solid lines), respectively. These oxygen mole fractions are chosen to illustrate the difference between Ga-rich mixtures [$x(O) = 0.2$] and Ga_2O_3 -rich mixtures [$x(O) = 0.4$].

vs. in the gas + Ga_2O_3 (s) regions differ by more than seven orders of magnitude, i.e., 6.4×10^{-24} Pa vs. 1.8×10^{-16} Pa as indicated by the brown and green common tangent lines in Fig. 4.

In Fig. 5(a) the partial pressure of oxygen in the gas phase is plotted as a function of temperature (for a total pressure of 0.1 Pa) for a Ga-rich mixture at $x(O) = 0.2$ and a Ga_2O_3 -rich mixture at $x(O) = 0.4$. It can be seen that the oxygen partial pressure in the Ga_2O_3 -rich mixture at $x(O) = 0.4$ is orders of magnitude higher than that at $x(O) = 0.2$ at relevant MBE growth temperatures. For example, the value of the partial pressures of oxygen at $T_{mix} = 1000$ K at $x(O) = 0.2$ is 5.6×10^{-25} Pa and at $x(O) = 0.4$ is 4.5×10^{-21} Pa. The higher oxygen activity of Ga_2O_3 -rich mixtures compared with Ga-rich mixtures makes it easier to form fully oxidized Ga_2O_3 thin films. At lower total pressure, all lines shift to lower temperatures.

Further, our thermodynamic calculations plotted in Fig. 5(b) show the ratio of the partial pressures of Ga_2O to Ga in the gas phase as a function of the temperature of a Ga-rich mixture [$x(O) = 0.2$] and of a Ga_2O_3 -rich mixture [$x(O) = 0.4$], where the total pressure is fixed at 0.1 Pa. The ratio of the partial pressures of Ga_2O to Ga in a Ga-rich mixture with $x(O) = 0.2$ is much lower than this ratio in a Ga_2O_3 -rich mixture with $x(O) = 0.4$. For example, the P_{Ga_2O}/P_{Ga} ratio is 158 in a Ga-rich mixture [$x(O) = 0.2$] and 1496 in a Ga_2O_3 -rich mixture [$x(O) = 0.4$] at $T_{mix} = 1000$ K. The higher Ga_2O/Ga ratios at higher T_{mix} are another reason why

Ga_2O_3 -rich mixtures are preferred. Higher Ga_2O/Ga ratios and the higher purity of the Ga_2O molecular-beam [99.98% Ga_2O according to our calculations at $x(O) = 0.4$] mean that the Ga_2O_3 films are formed by a single-step reaction [reaction (2)] and that reaction (1) is bypassed.

We used Ga metal (7N purity) and Ga_2O_3 powder (5N purity) for the Ga + Ga_2O_3 mixtures, loaded them into a 40 cm^3 Al_2O_3 crucible and inserted it into a commercial dual-filament, medium temperature MBE effusion cell. After mounting the effusion cell to our Veeco GEN10 MBE system and evacuating the source, we heated it up, outgassed the mixture, and set our desired Ga_2O flux for the growth of Ga_2O_3 . We measured the flux of the Ga_2O (g) molecular-beam reaching the growth surface prior to and after growth using a quartz crystal microbalance. The film surface was monitored during growth by reflection high-energy electron diffraction (RHEED) using 13 keV electrons. After growth x-ray reflectivity (XRR), optical reflectivity in a microscope (ORM),⁶² scanning electron microscopy (SEM), scanning transmission electron microscopy (STEM), and secondary-ion mass spectrometry (SIMS) were used to accurately measure the thicknesses of homoepitaxial (ORM, SEM, SIMS, SEM) and heteroepitaxial (XRR, ORM, SEM, STEM, SIMS) grown Ga_2O_3 films to determine the growth rate. X-ray diffraction was performed using a four-circle x-ray diffractometer with $Cu K\alpha_1$ radiation.

III. RESULTS FOR Ga_2O_3 USING S -MBE

A. Growth rates and growth model

Figure 6 plots the growth rate of Ga_2O_3 as a function of $\phi_{\text{Ga}_2\text{O}}$ at different T_G and constant ϕ_{O} . The growth rates obtained follow the anticipated growth kinetics depicted in Fig. 1(c). In the adsorption-controlled regime, an increase in $\phi_{\text{Ga}_2\text{O}}$ (at otherwise constant growth parameters) does *not* lead to a decrease in the growth rate as observed for ‘conventional’ Ga_2O_3 MBE [Fig. 1(b)],^{7,9} but instead results in a constant growth rate: a growth rate-plateau. The data clearly show that we have overcome the growth rate-limiting step by using a Ga_2O (g) suboxide molecular-beam while reducing the complexity of the Ga_2O_3 reaction kinetics from a two-step [Eqs. (1) and (2)] to a single-step [Eq. (2)] reaction mechanism.

The reaction kinetics of S -MBE for the growth of Ga_2O_3 (s) can be described in a similar way as ‘conventional’ III-V [e.g., reaction (3)] and II-VI MBE. We therefore set up a simple reaction-rate model describing the growth of Ga_2O_3 (s) by S -MBE (this same model applies to other III-VI and IV-VI compounds, as well):

$$\frac{dn_{\text{Ga}_2\text{O}}}{dt} = \phi_{\text{Ga}_2\text{O}} - \kappa_{\text{Ga}_2\text{O}} n_{\text{Ga}_2\text{O}} n_{\text{O}}^2 - \gamma_{\text{Ga}_2\text{O}} n_{\text{Ga}_2\text{O}}, \quad (9)$$

$$\frac{dn_{\text{O}}}{dt} = \sigma \phi_{\text{O}} - 2 \kappa_{\text{Ga}_2\text{O}} n_{\text{Ga}_2\text{O}} n_{\text{O}}^2 - \gamma_{\text{O}} n_{\text{O}}, \quad (10)$$

$$\frac{dn_{\text{Ga}_2\text{O}_3}}{dt} = \Gamma = \kappa_{\text{Ga}_2\text{O}} n_{\text{Ga}_2\text{O}} n_{\text{O}}^2. \quad (11)$$

The Ga_2O_3 , Ga_2O , and O adsorbate densities are denoted as $n_{\text{Ga}_2\text{O}_3}$, $n_{\text{Ga}_2\text{O}}$, and n_{O} , respectively. Their time derivative is described by the operator d/dt . The reaction rate constant $\kappa_{\text{Ga}_2\text{O}}$ kinetically describes the growth rate Γ of Ga_2O_3 (s) on the growth surface. The desorption rate constants of Ga_2O and O adsorbates are denoted as $\gamma_{\text{Ga}_2\text{O}}$ and γ_{O} , respectively.

The flux of available O adsorbates, for Ga_2O to Ga_2O_3 oxidation at a given T_G , is determined by its sticking coefficient σ on the Ga_2O_3 growth surface and is described by a sigmoid function

$$\sigma(T_G) = \left[\sigma_0 \exp\left(-\frac{\Delta\sigma}{k_B(T_G - dT_G)}\right) + 1 \right]^{-1}, \quad (12)$$

with dimensionless pre-factor σ_0 , energy $\Delta\sigma$, and temperature off-set dT_G . Equation (12) reflects the decreasing probability of O species to adsorb as T_G is increased. This leads to an effectively lower surface density of active O for Ga_2O oxidation and thus to lower growth rates.

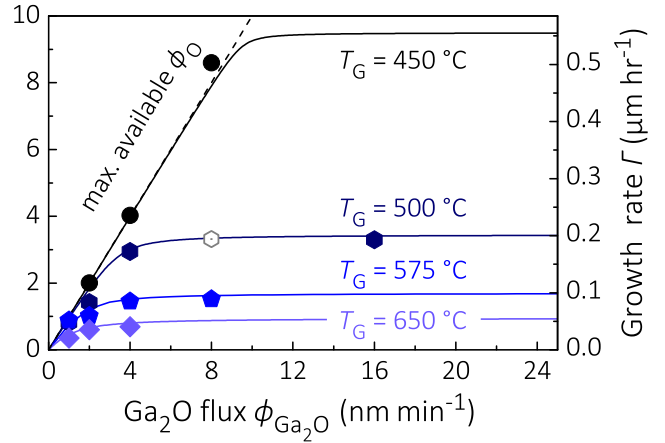


FIG. 6. Measured growth rate of $\text{Ga}_2\text{O}_3(\bar{2}01)/\text{Al}_2\text{O}_3(0001)$ as a function of $\phi_{\text{Ga}_2\text{O}}$ at different T_G (as indicated in the figure). Solid lines are fits of our model, Eqs. (9)–(11), to the data. A flux of ϕ_{O} was provided by an oxidant—a mixture of O_2 and approximately 80% O_3 ⁶³—supplied continuously during growth at a background pressure of 1×10^{-6} Torr. The dashed line reveals the transition between O-rich and Ga_2O -rich growth regimes and indicates the maximum available O flux (which equals the growth rate value of the plateau) for Ga_2O to Ga_2O_3 conversion at a given T_G .

For a supplied flux of ϕ_{O} corresponding to a background pressure of 1×10^{-6} Torr (involving mixtures of O_2 and approximately 10% O_3 as well as 80% O_3)⁶³, the values of the variables given in Eq. (12) are: $\sigma_0 = 40$, $\Delta\sigma = 29$ meV, and $dT_G = 675$ °C. In this work, we introduce this model for S -MBE to demonstrate its practical value. A physical description of this model including all model parameters is given in Ref. 64. The given values are extracted by fitting the maximum growth rate (defined as the plateau-regime) as a function of T_G , e.g., as plotted in Fig. 6. We find that σ does not depend on the concentration of active O; it only depends on the partial pressure of active O. Thus, the active O may be scaled up or down by either changing the concentration of O_3 in the O_3 beam or by changing the partial pressure of O_3 in the chamber. Note that O_3 supplies O to the surface of the growing film when it decomposes by the reaction: $\text{O}_3(g) \rightarrow \text{O}_2(g) + \text{O}(g)$. A similar behavior of an increasing desorption or recombination rate of active O species with increasing T_G has also been observed during O plasma-assisted MBE using elemental Ga and O molecular-beams.^{9,12,13}

Based on this model, we scaled up ϕ_{O} in order to achieve Ga_2O_3 (s) growth rates that exceed $1 \mu\text{m hr}^{-1}$. Figure 7(a) demonstrates our fastest (to date) growth rate of $1.6 \mu\text{m hr}^{-1}$ of a β - Ga_2O_3 thin film grown on $\text{Al}_2\text{O}_3(0001)$,

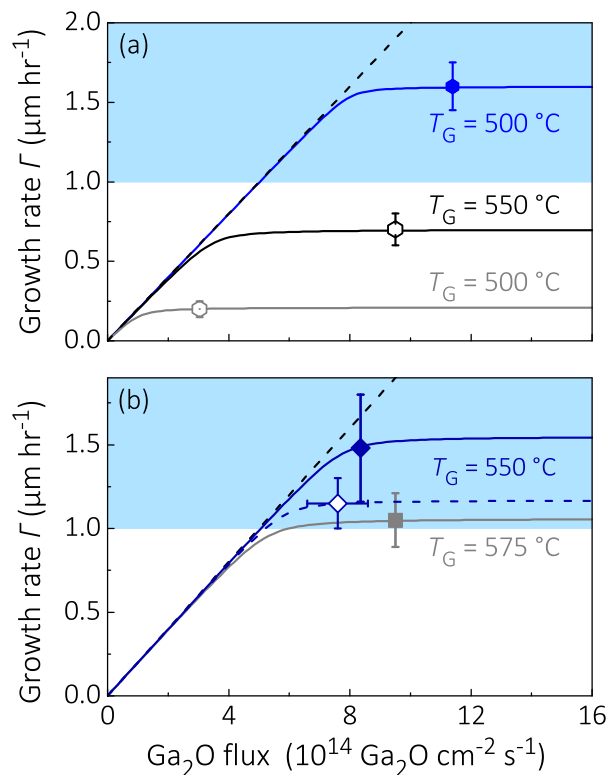


FIG. 7. (a) Examples of measured growth rates of $1.6 \mu\text{m hr}^{-1}$ (solid hexagon), $0.7 \mu\text{m hr}^{-1}$ (open hexagon), and $0.2 \mu\text{m hr}^{-1}$ (open-dotted hexagon; the same data point is shown in Fig. 6 in nm min^{-1}) of $\text{Ga}_2\text{O}_3(\bar{2}01)$ grown on $\text{Al}_2\text{O}_3(0001)$ at $\phi_{\text{Ga}_2\text{O}}$ of 11.4 , 9.5 , and $3.0 \times 10^{14} \text{ Ga}_2\text{O molecules cm}^{-2} \text{ s}^{-1}$, respectively. The oxygen flux was provided by an oxidant ($\text{O}_2 + 80\% \text{ O}_3$) background pressure of $5 \times 10^{-6} \text{ Torr}$ (solid hexagon and open hexagon) as well as $1 \times 10^{-6} \text{ Torr}$ (open-dotted hexagon). (b) Examples of measured growth rates of $1.5 \mu\text{m hr}^{-1}$ (solid diamond), $1.17 \mu\text{m hr}^{-1}$ (open diamond), and $1.05 \mu\text{m hr}^{-1}$ (solid square) of $\text{Ga}_2\text{O}_3(010)$ grown on $\text{Ga}_2\text{O}_3(010)$ at $\phi_{\text{Ga}_2\text{O}}$ of 8.4 , 7.6 , and $9.5 \times 10^{14} \text{ Ga}_2\text{O molecules cm}^{-2} \text{ s}^{-1}$, respectively. The oxygen flux was provided by an oxidant ($\text{O}_2 + 80\% \text{ O}_3$) background pressure of $5 \times 10^{-6} \text{ Torr}$. Growth temperatures, T_G , are indicated in the figure. Lines are estimations from our model, Eqs. (9)–(11), including all kinetic parameters⁶⁴. The dashed line shows the estimated intersection between the O-rich to the Ga_2O -rich growth regime⁶⁴. The blue shaded area indicates the adsorption-controlled growth rate-regime only accessible by *S*-MBE with growth rates $\geq 1 \mu\text{m hr}^{-1}$.

at $T_G = 500^\circ\text{C}$. For comparison, the data point plotted as an open-dotted hexagon (see also Fig. 6) shows the highest possible growth rate at a five times lower active ϕ_{O} and the same T_G . This result shows quite clearly the accuracy of our model and demonstrates the *S*-MBE of Ga_2O_3 thin films at growth rates exceeding $1 \mu\text{m hr}^{-1}$. In

addition, the growth rate values plotted in Fig. 7(b) were obtained by homoepitaxial growth of $\beta\text{-Ga}_2\text{O}_3(010)$ on $\beta\text{-Ga}_2\text{O}_3(010)$. The growth rate of Ga_2O_3 on $\text{Ga}_2\text{O}_3(010)$ is 2.1 times larger than the growth rate on $\text{Al}_2\text{O}_3(0001)$ at similar growth conditions—e.g., as plotted in Figs. 7(a) [open hexagon] and 7(b) [solid diamond], respectively. This result suggests that the growth rate of *S*-MBE grown $\text{Ga}_2\text{O}_3(010)$ and other surfaces of Ga_2O_3 may vastly exceed $1 \mu\text{m hr}^{-1}$ in the adsorption-controlled regime. The higher growth rate is likely due to the surface-dependent adhesion energies between of Ga_2O adsorbates and substrate^{11,12,65}, similar to what has been observed for Ga adsorbates during the ‘conventional’ MBE of Ga_2O_3 ⁴⁵. Fluctuations in T_G and $\phi_{\text{Ga}_2\text{O}}$ for different samples and during the long duration growth of the ‘thick’ sample (> 3 hours) are considered by the standard deviations of the measured values of T_G and $\phi_{\text{Ga}_2\text{O}}$ as given in Fig. 7.

B. Structural properties

We investigated the impact of variable growth conditions (i.e., $\phi_{\text{Ga}_2\text{O}}$, ϕ_{O} , and T_G) on the structural perfection of epitaxial Ga_2O_3 (*s*) films grown on $\text{Al}_2\text{O}_3(0001)$ and $\text{Ga}_2\text{O}_3(010)$ substrates. Figure 8 shows θ - 2θ x-ray diffraction (XRD) scans of selected Ga_2O_3 films—the same samples depicted in Fig. 7(a) [solid blue hexagon and open-dotted hexagon]. The reflections of the films coincide with the $\beta\text{-Ga}_2\text{O}_3$ phase grown with their $(\bar{2}01)$ plane parallel to the (0001) plane of the Al_2O_3 substrate. The inset shows transverse scans (rocking curves) across the symmetric $\bar{4}02$ reflection of the same layers. The full width at half maxima (FWHM) in ω of the profiles are a measure of the out-of-plane mosaic spread of the Ga_2O_3 layer. The obtained $\Delta\omega = 0.11^\circ \approx 400''$ (arcseconds) does not change with growth rate and is particularly remarkable since $\beta\text{-Ga}_2\text{O}_3(\bar{2}01)$ films grown on $\text{Al}_2\text{O}_3(0001)$, using elemental Ga^{7,67} or compound Ga_2O_3 sources²⁷, usually show much broader line profiles in their out-of-plane crystal distributions (from $\Delta\omega \approx 0.23^\circ$ ²⁷ to $\Delta\omega \sim 1.00^\circ$ ⁷). Thus, the profiles in Fig. 8 reveal a well-oriented and high quality epitaxial $\text{Ga}_2\text{O}_3(\bar{2}01)$ thin film. Furthermore, reflection high-energy electron diffraction (RHEED) and XRR measurements reveal a sharp and well-defined interface between $\text{Ga}_2\text{O}_3(\bar{2}01)$ and Al_2O_3 as well as a relatively smooth surface morphology obtained by *S*-MBE. We note that in the highly adsorption-controlled regime at lower T_G the accumulation of Ga_2O

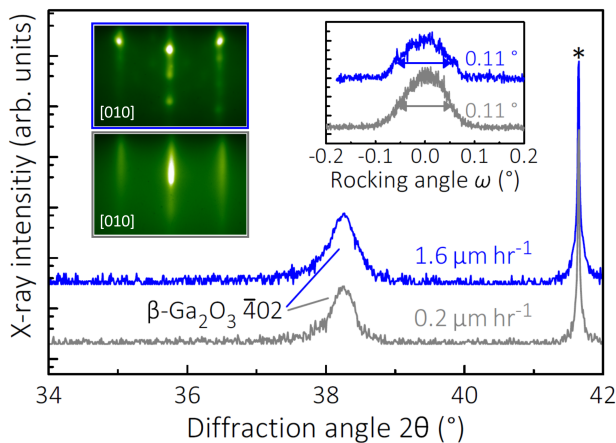


FIG. 8. Longitudinal XRD scans recorded for Ga_2O_3 films grown on $\text{Al}_2\text{O}_3(0001)$ single-crystal substrates in the adsorption-controlled regime. The blue line corresponds to a film with thickness of $d = 0.15 \mu\text{m}$ grown at $\phi_{\text{Ga}_2\text{O}} = 11.4 \times 10^{14} \text{ Ga}_2\text{O molecules cm}^{-2} \text{ s}^{-1}$ where ϕ_{O} was provided by an oxidant ($\text{O}_2 + 80\% \text{ O}_3$) background pressure of 5×10^{-6} Torr [see also solid blue hexagon in Fig. (7)(a)]. The gray line corresponds to a Ga_2O_3 film with thickness $d = 0.05 \mu\text{m}$ grown at $\phi_{\text{Ga}_2\text{O}} = 3.0 \times 10^{14} \text{ Ga}_2\text{O molecules cm}^{-2} \text{ s}^{-1}$ where ϕ_{O} was provided by an oxidant ($\text{O}_2 + 80\% \text{ O}_3$) background pressure of 1×10^{-6} Torr [see also gray open-dotted hexagon in Fig. (7)(a)]. For both samples T_G was 500°C . The reflections from the Ga_2O_3 film are identified to originate from the monoclinic β -phase,⁶⁶ as indicated in the figure. (Inset) Transverse XRD scans across the $\bar{4}02$ peak with their FWHM indicated in the figure (same value for both films). The 0006 peaks of the Al_2O_3 substrates are marked by an asterisk. RHEED images taken at the end of the growth along the $[010]$ azimuth of the Ga_2O_3 films grown at growth rates of $1.6 \mu\text{m hr}^{-1}$ and $0.2 \mu\text{m hr}^{-1}$ are outlined by the blue and gray boxes, respectively.

adsorbates (crystallites) on the growth surface may occur, similar to the formation of Ga droplets during GaN growth³⁶. This effect is indicated by the slightly spotty RHEED image (outlined by the blue square) in Fig. 8. We have not yet optimized the growth for $\text{Ga}_2\text{O}_3(\bar{2}01)$ films on $\text{Al}_2\text{O}_3(0001)$ with thicknesses $\gg 1 \mu\text{m}$ and mapped all growth regimes (e.g., Ga_2O ‘droplet’ formation at very high $\phi_{\text{Ga}_2\text{O}}$). Further investigations of the structural perfection and electrical properties of Ga_2O_3 grown by S -MBE need to be performed. This could be particularly interesting for the the growth of $\text{Ga}_2\text{O}_3(s)$ at even higher $\text{Ga}_2\text{O}(g)$ fluxes, which push even further into the adsorption-controlled regime.

We performed S -MBE for homoepitaxial β - $\text{Ga}_2\text{O}_3(010)$ films grown on β - $\text{Ga}_2\text{O}_3(010)$ substrates. Figure

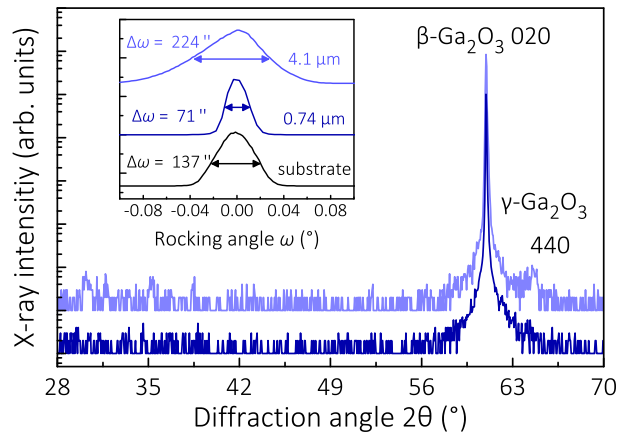


FIG. 9. Longitudinal XRD scans recorded for Ga_2O_3 films grown on $\text{Ga}_2\text{O}_3(010)$ single-crystal substrates in the adsorption-controlled regime. The pale blue and dark blue lines correspond to Ga_2O_3 films with thicknesses of $d = 4.1 \mu\text{m}$ and $d = 0.74 \mu\text{m}$, respectively. The reflections of the films coincide with the β - $\text{Ga}_2\text{O}_3(010)$ phase grown with their (010) plane parallel to the plane of the substrate. (Inset) Transverse scans across the 020 peak of the same samples with their FWHM indicated in the figure. For comparison, a transverse scan of a single-crystalline $\text{Ga}_2\text{O}_3(010)$ substrate is also shown. The $\text{Ga}_2\text{O}_3(010)$ films (pale blue and dark blue) were grown at $\phi_{\text{Ga}_2\text{O}} = 9.1 \times 10^{14} \text{ Ga}_2\text{O molecules cm}^{-2} \text{ s}^{-1}$ and $T_G = 550^\circ\text{C}$ where ϕ_{O} was provided by an oxidant ($\text{O}_2 + 80\% \text{ O}_3$) background pressure of 5×10^{-6} Torr. The surface morphologies of the ‘thin’ ($d = 0.74 \mu\text{m}$) and ‘thick’ ($d = 4.1 \mu\text{m}$) $\text{Ga}_2\text{O}_3(010)$ films are depicted in Figs. 11(a) and 11(b). The growth rates of the ‘thin’ and ‘thick’ films are depicted by the solid and open diamonds, respectively, in Fig. 7(b).

9 shows the θ - 2θ XRD scans of two selected $\text{Ga}_2\text{O}_3(010)$ films grown under the same growth conditions. The θ - 2θ XRD profiles of the $\text{Ga}_2\text{O}_3(010)$ film with thickness $d = 0.74 \mu\text{m}$ (plotted in dark blue) and the one of the substrate (data not shown) coincide. The $\text{Ga}_2\text{O}_3(010)$ layer with $d = 4.1 \mu\text{m}$ (depicted as pale blue) also shows small contributions of the meta stable γ - Ga_2O_3 phase. The inset of Fig. 9 shows the respective rocking curves across the symmetric 020 reflections of the same films as plotted in the main graph of Fig. 9. The obtained FWHM of the rocking curve of the film with $d = 0.74 \mu\text{m}$ is comparable to the one obtained for the bare $\text{Ga}_2\text{O}_3(010)$ substrate (depicted as a black line). [Note that the measured XRD spectra were obtained on different $10 \times 10 \text{ mm}^2$ substrates which were all cut from the same 1" diameter $\text{Ga}_2\text{O}_3(010)$ wafer from Synoptics.] The rocking curve of the ‘thick’ film with $d = 4.1 \mu\text{m}$ is considerably broader than the rocking curve detected for the ‘thin’

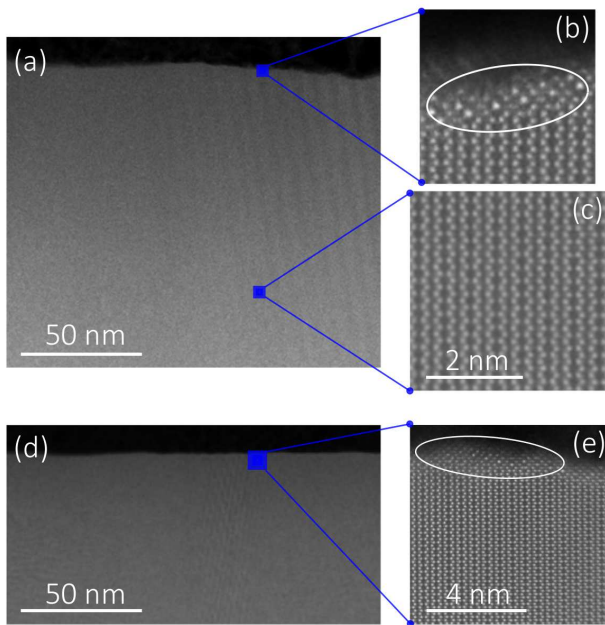


FIG. 10. (a)–(c) STEM images along the [001] zone axis of a $\text{Ga}_2\text{O}_3(010)$ ‘thin’ film grown at a growth rate of $1.05 \mu\text{m hr}^{-1}$ with thickness $d = 0.28 \mu\text{m}$ [this is the same sample depicted by the solid square in Fig. 7(b)]. The surface morphology of this same sample is shown in Fig. 11(c). (d)–(e) STEM images of a $\text{Ga}_2\text{O}_3(010)$ ‘thick’ film at growth rate of $1.17 \mu\text{m hr}^{-1}$ with thickness $4.1 \mu\text{m}$ [this is the same sample depicted by the open diamond in Fig. 7(b) and pale blue line in Fig. 9]. The surface morphology of this film is depicted in Fig. 11(b). No large-scale defects or dislocations are observed within either layers [panels (a) and (d)]. The Ga_2O_3 films consist only of the $\beta\text{-Ga}_2\text{O}_3(010)$ phase [panel (c) and (e)], except for a thin $\gamma\text{-Ga}_2\text{O}_3$ phase at the top surface [highlighted by a white circle in (b) and (e)].

$\text{Ga}_2\text{O}_3(010)$ film with $d = 0.74 \mu\text{m}$. We attribute the different rocking curve widths measured to the non-uniformity in the crystalline perfection across the 1" diameter Ga_2O_3 substrate on which these measurements were made.

STEM of a ‘thin’ $\text{Ga}_2\text{O}_3(010)$ film with $d = 0.28 \mu\text{m}$ (grown under similar conditions as the samples shown in Fig. 9) and the ‘thick’ film with $d = 4.1 \mu\text{m}$ (same sample as plotted as pale blue line in Fig. 9) are shown in Figs. 10(a)–10(c) and Figs. 10(d)–10(e), respectively. Both samples show a clear, uniform, and single-crystalline $\beta\text{-Ga}_2\text{O}_3(010)$ film. The vertical banding in Figs. 10(a) and 10(d) are moiré fringes between the in-focus portion of the crystal lattice and the finite pixel sampling of the STEM image. Defects such as dislocations or strain fields would have distorted the fringes away from straight lines, indicating an absence of such fea-

tures. Only a thin $\sim 1 \text{ nm}$ thick $\gamma\text{-Ga}_2\text{O}_3(110)$ phase at the top of the surfaces of their $\text{Ga}_2\text{O}_3(010)/\text{Ga}_2\text{O}_3(010)$ structures can be seen, as marked by white circles in Figs. 10(b) and 10(e).

The surface morphology of $\text{Ga}_2\text{O}_3(010)$ films grown by *S*-MBE at growth rates $> 1 \mu\text{m hr}^{-1}$ were investigated by atomic force microscopy (AFM) and are plotted in Figs. 11(a)–11(c). The root mean square (rms) roughness of the ‘thin’ film with $d = 0.74 \mu\text{m}$ is lower than the one measured for the ‘thick’ film with $d = 4.1 \mu\text{m}$. This evolution in rms roughness follows the same trend as observed by XRD scans of the same layers (dark blue and pale blue lines in the inset of Fig. 9), i.e., a slight decrease in crystal quality with increasing film thickness of the $\text{Ga}_2\text{O}_3(010)/\text{Ga}_2\text{O}_3(010)$ structures.

C. Impurities

We investigated the incorporation of impurities into the $\text{Ga}_2\text{O}_3(010)$ thin films grown with growth rates $> 1 \mu\text{m hr}^{-1}$ by SIMS. Figure 12 shows the SIMS profile of the same film as plotted in Figs. 7 (solid square), Fig. 10, and Fig. 11(c). This profile reveals that the Ga_2O_3 -rich ($\text{Ga} + \text{Ga}_2\text{O}_3$) mixtures employed lead to $\text{Ga}_2\text{O}_3(010)$ thin films with low impurity incorporation. Only a slight increase of Al impurities with increasing film thickness and a slight incorporation of B are detected. These impurities likely originate from our use of an Al_2O_3 crucible for the Ga_2O_3 -rich ($\text{Ga} + \text{Ga}_2\text{O}_3$) mixture. We note that we have also used pyrolytic boron nitride (pBN) crucibles for the $\text{Ga} + \text{Ga}_2\text{O}_3$ mixture, but find high concentrations of B in the grown films by SIMS ($\sim 10^{20} \text{ B cm}^{-3}$) when the background pressure of a mixture of $\text{O}_2 + 80\% \text{O}_3$ is $P_{\text{O}} = 5 \times 10^{-6} \text{ Torr}$. We attribute this to the oxidation of the surface of the pBN crucible to B_2O_3 at the high oxidant pressures used. At the $T_{\text{mix}} = 1020 \text{ }^\circ\text{C}$ used for growth, the vapor pressure of B_2O_3 is significant.⁵⁵ The small Si peak measured at the film-substrate interface originates from unintentional incorporated Si at the substrate surface. Note, we have tried Ga_2O -polishing (for the first time) to remove the Si from the surface prior to growth. Our observation is that Ga_2O -polishing does not provide the same reduction in Si contamination at the sample surface as can be accomplished by Ga-polishing.⁶⁸

Our SIMS results show that the low effusion cell temperatures and Ga_2O_3 -rich ($\text{Ga} + \text{Ga}_2\text{O}_3$) mixtures employed for *S*-MBE—in order to produce such high Ga_2O fluxes to

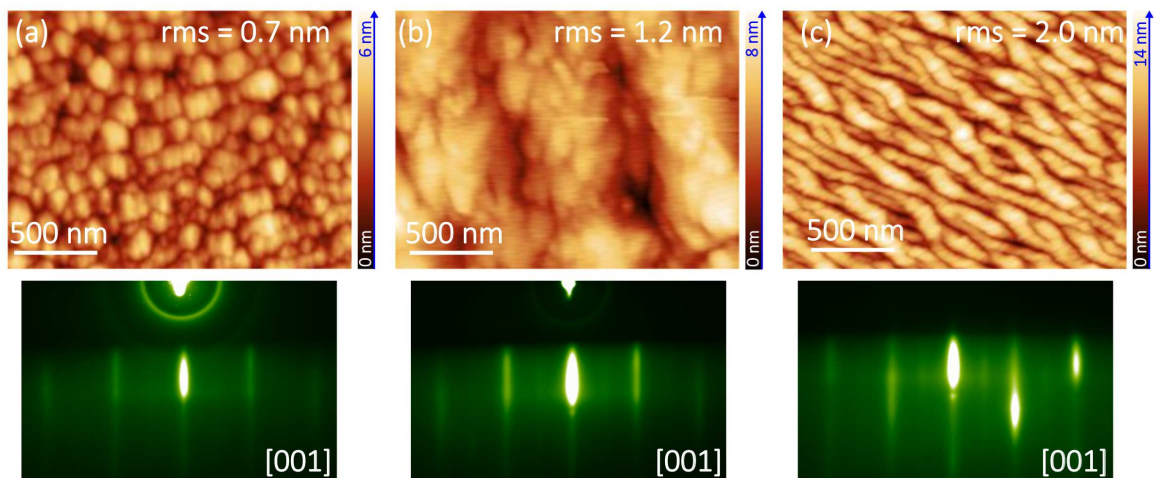


FIG. 11. (a)–(c) Surface morphologies obtained by AFM for $\text{Ga}_2\text{O}_3(010)$ surfaces grown by *S*-MBE. The rms roughness of the surfaces are indicated on the figures. The XRD patterns of the same layers as shown in (a) and (b) are plotted in Fig. 9 as dark blue and pale blue lines, respectively. The growth rates of the films shown in (a), (b) and (c), are depicted in Fig. 7 as solid diamond, open diamond, and solid square, respectively. The thicknesses of the films in (a) and (c) are $d = 0.74 \mu\text{m}$ and the thickness of the film with the morphology shown in (b) is $d = 4.1 \mu\text{m}$. T_G was set to 550°C for the films shown in (a) and (b) and to $T_G = 575^\circ\text{C}$ for the film plotted in (c). RHEED images of the corresponding Ga_2O_3 film taken at the end of growth along the $[001]$ azimuth are displayed below the respective AFM images.

grow Ga_2O_3 with growth rates exceeding $> 1 \mu\text{m hr}^{-1}$ —do not lead to significant impurity incorporation into the grown $\text{Ga}_2\text{O}_3(010)$ films. This is an advantage of *S*-MBE compared to the growth Ga_2O_3 from a crucible containing pure Ga_2O_3 . Using a Ga_2O_3 compound source at extremely high effusion cell temperatures ($\sim 1700^\circ\text{C}$)⁵⁶, not only produces

a flux containing a relatively low Ga_2O molecular-beam resulting in low Ga_2O_3 film growth rates, but also results in films contaminated with iridium.^{32,56,57} Nonetheless, electrical transport properties are extremely sensitive to impurities and measurements of mobility in doped Ga_2O_3 films grown by *S*-MBE remain to be performed. It could turn out that a higher purity Ga_2O_3 powder will be needed than the 5N Ga_2O_3 powder we have used in this study.

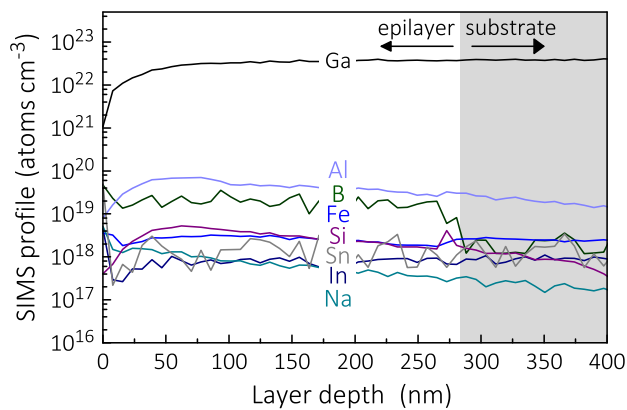


FIG. 12. SIMS of a $\text{Ga}_2\text{O}_3(010)$ thin film grown at $1.05 \mu\text{m hr}^{-1}$ [this is the same sample depicted by the solid square in Fig. 7(b)]. The atomic structure of this film and its surface morphology are shown in Figs. 10(a)–10(c) and 11(c), respectively. No significant impurity incorporation could be detected. Gray and white areas show the SIMS profile of the $\text{Ga}_2\text{O}_3(010)$ thin film and the Fe-doped $\text{Ga}_2\text{O}_3(010)$ substrate, respectively.

D. Summary

The growth rates we have achieved by *S*-MBE are more than one order of magnitude faster than what has been reported for the growth of Ga_2O_3 films from pure Ga_2O_3 sources.³²

The quality of the homoepitaxial $\beta\text{-Ga}_2\text{O}_3(010)$ films (with thickness $> 4 \mu\text{m}$) assessed by XRD (Fig. 9), STEM (Fig. 10), AFM (Fig. 11) and SIMS (Fig. 12), reveal that *S*-MBE with growth rates $> 1 \mu\text{m hr}^{-1}$ is competitive to other industrial relevant synthesis methods [such as (MO)CVD] for the growth of vertical Ga_2O_3 -based structures with thicknesses in the μm -range.

Based on our model and experimental results, we anticipate growth rates up to $5 \mu\text{m hr}^{-1}$ on $\text{Ga}_2\text{O}_3(010)$ and other growth surfaces to be possible by *S*-MBE. This estima-

tion is based on the physical MBE limit: the mean free path λ of the species (e.g., Ga₂O and O₃) emanating from their sources to the target. In our estimate we have used an upper limit for the O partial pressure of $P_{\text{O}} \sim 2 \times 10^{-4}$ Torr [resulting in $\lambda \sim 0.1$ m]⁶⁹ and a lower T_G limit of $T_G \geq 725$ °C [required for the adsorbed species (e.g., Ga₂O and O) to crystallize into a homoepitaxial film of Ga₂O₃].

IV. OUTLOOK AND ALTERNATIVES OF *S*-MBE

We have demonstrated the growth of high quality Ga₂O₃ (*s*) thin films by *S*-MBE in the adsorption-controlled regime using Ga (*l*) + Ga₂O₃ (*s*) mixtures. The high growth rate $\gg 1 \mu\text{m hr}^{-1}$, and unparalleled crystal quality of the homoepitaxial and heteroepitaxial structures obtained (with $d \gg 1 \mu\text{m}$) suggest the possibility of unprecedented mobilities of Ga₂O₃ thin films containing *n*-type donors (Sn, Ge, Si) grown by *S*-MBE.

We have also developed Sn + SnO₂ and Ge + GeO₂ mixtures in order to produce SnO (*g*) and GeO (*g*) beams for use as *n*-type donors in Ga₂O₃-based heterostructures. Furthermore, we have grown SnO₂ using a Sn + SnO₂ mixture.³¹ Moreover, we have grown Ga₂O₃ doped with SnO using Ga₂O and SnO beams and achieved controllable Sn-doping levels in these Ga₂O₃ films.⁷⁰ Nevertheless, the improvement of the *n*-type mobilities obtained during *S*-MBE, at growth rates $> 1 \mu\text{m hr}^{-1}$, still needs to be demonstrated and shown to exceed the state-of-the-art mobilities in Ga₂O₃ films grown by ‘conventional’ MBE.⁷¹

Our comprehensive thermodynamic analysis of the volatility of 128 binary oxides plus additional two-phase mixtures of metals with their binary oxides,⁵⁵ e.g., Ga + Ga₂O₃, have led us to recognize additional systems appropriate for growth by *S*-MBE. This thermodynamic knowledge coupled with our understanding of the *S*-MBE growth of Ga₂O₃ enabled us to develop In + In₂O₃ and Ta + Ta₂O₅ mixtures from which we have grown high-quality bixbyite In₂O₃^{64,72} and In₂O₃:SnO₂ (ITO, with up to 30% Sn)^{64,72} as well as rutile TaO₂⁷³ by *S*-MBE, respectively.

Growing thin films with very high crystalline qualities at growth rates $> 1 \mu\text{m hr}^{-1}$ by using suboxide molecular-beams—with up to $5 \mu\text{m hr}^{-1}$ anticipated growth rates by our model—will make MBE competitive to other established synthesis methods, such as CVD³³ or MOVPE.³⁴ The T_G that we have demonstrated for high quality Ga₂O₃ layers grown by *S*-MBE is significantly lower than what has been demon-

strated for the growth of high quality Ga₂O₃ films by CVD or MOVPE. This makes *S*-MBE advantageous for BEOL processing. Additionally, Ga₂O₃ grown with a vast excess of Ga₂O (*g*) and high oxygen activity in Ga₂O₃-rich mixtures may suppress Ga vacancies in the Ga₂O₃ layers formed, which are believed to act as compensating acceptors^{20,74}—potentially improving the electrical performance of *n*-type Ga₂O₃-based devices significantly.

The development of Al + Al₂O₃ mixtures for the growth of epitaxial Al₂O₃ and (Al_{*x*}Ga_{1-*x*})₂O₃ at comparably high growth rates by *S*-MBE is foreseeable. In order to fabricate vertical high-power devices, thin film thicknesses in the micrometer range are desired. *S*-MBE allows the epitaxy of such devices in relatively short growth times (i.e., within a few hours as demonstrated for Ga₂O₃(010) in this work) while maintaining nanometer scale smoothness. In addition, the use of a Al₂O (*g*) and Ga₂O (*g*) molecular-beams during (Al_{*x*}Ga_{1-*x*})₂O₃ *S*-MBE may also extend its growth domain towards higher adsorption-controlled regimes—being beneficial for the performance of (Al_{*x*}Ga_{1-*x*})₂O₃-based heterostructure devices.

Our demonstration of high quality films of Ga₂O₃, Ga₂O₃ doped with SnO,⁷⁰ In₂O₃,^{64,72} ITO,^{64,72} TaO₂,⁷³ LaInO₃,⁷⁵ and LaAlO₃,⁷⁶ suggests that this synthesis-science approach—utilizing a combination of thermodynamics to identify which suboxides can be produced in molecular-beams in combination with a kinetic model of the growth process—can be applied to a wide-range of oxide compounds.⁵⁵ We anticipate *S*-MBE to be applicable to all materials that form via intermediate reaction products (a *subcompound*). Examples following this reasoning include ZrO₂, Pb(Zr,Ti)O₃, and (Hf,Zr)O₂ all via the supply of a molecular-beam of ZrO (predicted by our thermodynamic calculations,⁵⁵) Ga₂Se₃ via Ga₂Se,^{11,77,78} In₂Se₃ through In₂Se,^{11,79,80} In₂Te₃ by In₂Te,^{11,81} or Sn₂Se via SnSe.^{11,82}

V. ACKNOWLEDGMENTS

We thank J. D. Blevins for the Ga₂O₃(010) substrates from Synoptics, Inc. used in this study. K. A., C. S. C., J. P. M., D. J., H. G. X., D. A. M., and D. G. S. acknowledge support from the AFOSR/AFRL ACCESS Center of Excellence under Award No. FA9550-18-1-0529. J. P. M. also acknowledges from National Science Foundation within a Graduate Research Fellowship under Grant No. DGE-1650441. P. V. acknowledges support from ASCENT, one

of six centers in JUMP, a Semiconductor Research Corporation (SRC) program sponsored by DARPA. F. V. E. H. acknowledges support from the Alexander von Humboldt foundation in form of a Feodor Lynen fellowship. F.V.E.H and H. P. acknowledge support from the National Science Foundation (NSF) [Platform for the Accelerated Realization, Analysis and Discovery of Interface Materials (PARADIM)] under Cooperative Agreement No. DMR-1539918. J. P. acknowledges support from the Air Force Office of Scientific Research under Award No. FA9550-20-1-0102. S. L. S. and Z. K. L. acknowledge the support of NSF through Grant No. CMMI-1825538. This work made use of the Cornell Center for Materials Research (CCMR) Shared Facilities, which are supported through the NSF MRSEC Program (No. DMR-1719875). Substrate preparation was performed in part at the Cornell NanoScale Facility, a member of the National Nanotechnology Coordinated Infrastructure (NNCI), which is supported by the NSF (Grant No. ECCS-1542081).

Competing interests: The authors P. V., D. G. S., F. V. E. H., K. A., Z.-K. L., B. J. B., S.-L. S., Cornell University (D-9573) and the Pennsylvania State University (2020-5155) have filed a patent entitled: Adsorption-Controlled Growth of Ga₂O₃ by Suboxide Molecular-Beam Epitaxy.

VI. DATA AVAILABILITY

No data that support the findings in this study are required and provided.

- ¹M. A. Hermann and A. Sitter, *Molecular Beam Epitaxy: Fundamentals and Current Status, 2nd Edition* (Springer, Berlin, 1996) pp. 1–31.
- ²T. Onuma, S. Saito, K. Sasaki, T. Masui, T. Yamaguchi, T. Honda, and M. Higashiwaki, *Jpn. J. Appl. Phys.* **54**, 112601 (2015).
- ³T. Wang, W. Li, C. Ni, and A. Janotti, *Phys. Rev. Applied* **10**, 011003 (2018).
- ⁴M. Higashiwaki, K. Sasaki, A. Kuramata, T. Masui, and S. Yamakoshi, *Appl. Phys. Lett.* **100**, 013504 (2012).
- ⁵S. Krishnamoorthy, Z. Xia, C. Joishi, Y. Zhang, J. McGlone, J. Johnson, M. Brenner, A. R. Arehart, J. Hwang, S. Lodha, and S. Rajan, *Appl. Phys. Lett.* **111**, 023502 (2017).
- ⁶R. Jinno, C. S. Chang, T. Onuma, Y. Cho, S.-T. Ho, M. C. Cao, K. Lee, V. Protasenko, D. G. Schlom, D. A. Muller, H. G. Xing, and D. Jena, arXiv: 2007.03415 (2020).
- ⁷M.-Y. Tsai, O. Bierwagen, M. E. White, and J. S. Speck, *J. Vac. Sci. Technol. A* **28**, 354 (2010).
- ⁸P. Vogt and O. Bierwagen, *Appl. Phys. Lett.* **106**, 081910 (2015).
- ⁹P. Vogt and O. Bierwagen, *Appl. Phys. Lett.* **108**, 072101 (2016).
- ¹⁰P. Vogt, O. Brandt, H. Riechert, J. Lähnemann, and O. Bierwagen, *Phys. Rev. Lett.* **119**, 196001 (2017).
- ¹¹P. Vogt and O. Bierwagen, *Phys. Rev. Mater.* **2**, 120401(R) (2018).
- ¹²P. Vogt, *Growth Kinetics, Thermodynamics, and Phase Formation of group-III and IV oxides during Molecular Beam Epitaxy*, Ph.D. thesis, Humboldt University of Berlin (2017).
- ¹³P. Vogt and O. Bierwagen, *Appl. Phys. Lett.* **109**, 062103 (2016).
- ¹⁴S. Migita, Y. Kasai, H. Ota, and S. Sakai, *Appl. Phys. Lett.* **71**, 3712 (1997).
- ¹⁵R. W. Ulbricht, A. Schmehl, T. Heeg, J. Schubert, and D. G. Schlom, *Appl. Phys. Lett.* **93**, 102105 (2008).
- ¹⁶J. L. MacManus-Driscoll, M. P. Wells, C. Yun, J. W. Lee, C. B. Eom, and D. G. Schlom, *APL Mater.* **8**, 040904 (2020).
- ¹⁷O. Bierwagen, M. E. White, M. Y. Tsai, and J. S. Speck, *Appl. Phys. Lett.* **95**, 262105 (2009).
- ¹⁸H. Paik, Z. Chen, E. Lochocki, H. Ariel Seidner, A. Verma, N. Tanen, J. Park, M. Uchida, S. Shang, B. C. Zhou, M. Brützram, R. Uecker, Z. K. Liu, D. Jena, K. M. Shen, D. A. Muller, and D. G. Schlom, *APL Mater.* **5**, 116107 (2017).
- ¹⁹A. B. Mei, L. Miao, M. J. Wahila, G. Khalsa, Z. Wang, M. Barone, N. J. Schreiber, L. E. Noskin, H. Paik, T. E. Tiwald, Q. Zheng, R. T. Haasch, D. G. Sangiovanni, L. F. Piper, and D. G. Schlom, *Phys. Rev. Mater.* **3**, 105202 (2019).
- ²⁰E. Korhonen, F. Tuomisto, D. Gogova, G. Wagner, M. Baldini, Z. Galazka, R. Schewski, and M. Albrecht, *Appl. Phys. Lett.* **106**, 242103 (2015).
- ²¹H. Peelaers, J. L. Lyons, J. B. Varley, and C. G. Van De Walle, *APL Mater.* **7**, 022519 (2019).
- ²²E. Calleja, M. A. Sánchez-García, F. J. Sánchez, F. Calle, F. B. Naranjo, E. Muñoz, S. I. Molina, A. M. Sánchez, F. J. Pacheco, and R. García, *J. Cryst. Growth* **201**, 296 (1999).
- ²³G. Koblmüller, C. S. Gallinat, and J. S. Speck, *J. Appl. Phys.* **101**, 083516 (2007).
- ²⁴S. Fernández-Garrido, G. Koblmüller, E. Calleja, and J. S. Speck, *J. Appl. Phys.* **104**, 033541 (2008).
- ²⁵H. Kato, M. Sano, K. Miyamoto, and T. Yao, *Jpn. J. Appl. Phys.* **42**, 2241 (2003).
- ²⁶S. Ghose, M. S. Rahman, J. S. Rojas-Ramirez, M. Caro, R. Droopad, A. Arias, and N. Nedev, *J. Vac. Sci. Technol. B* **34**, 02L109 (2016).
- ²⁷S. Ghose, S. Rahman, L. Hong, J. S. Rojas-Ramirez, H. Jin, K. Park, R. Klie, and R. Droopad, *J. Appl. Phys.* **122**, 095302 (2017).
- ²⁸R. Droopad, *Private communication from Ravi Droopad, the corresponding author of Ref.²⁷* (2017).
- ²⁹R. H. Lamoreaux, D. L. Hildenbrand, and L. Brewer, *J. Phys. Chem. Ref. Data* **16**, 419 (1987).
- ³⁰C. J. Frosch and C. D. Thurmond, *J. Phys. Chem.* **66**, 877 (1962).
- ³¹G. Hoffmann, M. Budde, P. Mazzolini, and O. Bierwagen, *APL Mater.* **8**, 031110 (2020).
- ³²M. Passlack, Z. Yu, R. Droopad, J. K. Abrokwhah, D. Braddock, S.-I. Yi, M. Hale, J. Sexton, and A. C. Kummel, *Research Signpost, Kera la, India* (2003) pp. 1–29.
- ³³S. Rafique, L. Han, A. T. Neal, S. Mou, J. Boeckl, and H. Zhao, *Phys. Status Solidi A* **215**, 1700467 (2018).
- ³⁴Y. Zhang, F. Alema, A. Mauze, O. S. Koksaldi, R. Miller, A. Osinsky, and J. S. Speck, *APL Mater.* **7**, 022506 (2019).
- ³⁵P. Vogt, A. Mauze, F. Wu, B. Bonef, and J. S. Speck, *Appl. Phys. Express* **11**, 115503 (2018).
- ³⁶B. Heying, R. Aeverbeck, L. F. Chen, E. Haus, H. Riechert, and J. B. Speck, *Appl. Phys. Lett.* **88**, 1855 (2000).

- ³⁷N. Gogneau, E. Sarigiannidou, E. Monroy, S. Monnoye, H. Mank, and B. Daudin, *Appl. Phys. Lett.* **85**, 1421 (2004).
- ³⁸J. Neugebauer, T. K. Zywiets, M. Scheffler, J. E. Northrup, H. Chen, and R. M. Feenstra, *Phys. Rev. Lett.* **90**, 056101 (2003).
- ³⁹J. Kwo, M. Hong, A. R. Kortan, K. L. Queeney, Y. J. Chabal, R. L. Opila, D. A. Muller, S. N. Chu, B. J. Sapjeta, T. S. Lay, J. P. Mannaerts, T. Boone, H. W. Krautter, J. J. Krajewski, A. M. Sergnt, and J. M. Rosamilia, *J. Appl. Phys.* **89**, 3920 (2001).
- ⁴⁰O. Bierwagen, A. Proessdorf, M. Niehle, F. Grosse, A. Trampert, and M. Klingsporn, *Cryst. Growth Des.* **13**, 3645 (2013).
- ⁴¹A. Fissel, Z. Elassar, O. Kirfel, E. Bugiel, M. Czernohorsky, and H. J. Osten, *J. Appl. Phys.* **99**, 074105 (2006).
- ⁴²J. P. Liu, P. Zaumseil, E. Bugiel, and H. J. Osten, *Appl. Phys. Lett.* **79**, 671 (2001).
- ⁴³T. Watahiki, W. Braun, and H. Riechert, *J. Vac. Sci. Technol. B* **27**, 262 (2009).
- ⁴⁴C. P. Chen, M. Hong, J. Kwo, H. M. Cheng, Y. L. Huang, S. Y. Lin, J. Chi, H. Y. Lee, Y. F. Hsieh, and J. P. Mannaerts, *J. Cryst. Growth* **278**, 638 (2005).
- ⁴⁵K. Sasaki, A. Kuramata, T. Masui, E. G. Villora, K. Shimamura, and S. Yamakoshi, *Appl. Phys. Express* **5**, 035502 (2012).
- ⁴⁶S. Raghavan, T. Schumann, H. Kim, J. Y. Zhang, T. A. Cain, and S. Stemmer, *APL Mater.* **4**, 016106 (2016).
- ⁴⁷G. Hass, *J. Am. Ceram. Soc.* **33**, 353 (1950).
- ⁴⁸M. Fernández-Perea, M. Vidal-Dasilva, J. I. Larruquert, J. A. Aznárez, J. A. Méndez, E. Gullikson, A. Aquila, and R. Soufli, *J. Appl. Phys.* **105**, 353 (2009).
- ⁴⁹J. Geurts, S. Rau, W. Richter, and F. J. Schmitte, *Thin Solid Films* **121**, 217 (1984).
- ⁵⁰V. Krávec, Z. Škraba, M. Hudomalj, and S. Sulčič, *Thin Solid Films* **129**, L61 (1985).
- ⁵¹X. Q. Pan and L. Fu, *J. Appl. Phys.* **89**, 6048 (2001).
- ⁵²X. Q. Pan and L. Fu, *J. Electroceram.* **7**, 35 (2001).
- ⁵³W. Guo, L. Fu, Y. Zhang, K. Zhang, L. Y. Liang, Z. M. Liu, H. T. Cao, and X. Q. Pan, *Appl. Phys. Lett.* **96**, 042113 (2010).
- ⁵⁴B. Gorbunov, V. Y. Filipchenko, and S. K. Finkel'shtein, *Inorg. Mater.* **19**, 1239 (1983).
- ⁵⁵K. M. Adkison, S.-L. Shang, B. J. Bocklund, D. Klimm, D. G. Schlom, and Z.-K. Liu, *APL Mater.* **8**, 081110 (2020).
- ⁵⁶M. Passlack, J. K. Abrokwah, and Z. J. Yu, *United States Patent* **6,094,295** (2000).
- ⁵⁷M. Passlack, J. K. Abrokwah, R. Droopad, and C. D. Overgaard, *United States Patent* **6,030,453** (2000).
- ⁵⁸C. B. Alcock, V. P. Itkin, and M. K. Horrigan, *Can. Metall. Quart.* **23**, 309 (1984).
- ⁵⁹M. Zinkevich and F. Aldinger, *J. Am. Ceram. Soc.* **87**, 683 (2004).
- ⁶⁰Scientific Group Thermodata Europe (SGTE), in *Landolt-Boernstein New Ser. Gr. IV*, edited by Lehrstuhl fuer Theoretische Huettenkunde (Springer, Verlag Berlin Heidelberg, 1999).
- ⁶¹J.-O. Andersson, T. Helander, L. Höglund, S. Pingfang, and B. Sundman, *Calphad* **26**, 273 (2002).
- ⁶²*FilMetrics F40*, KLA Corporation (San Diego, CA).
- ⁶³C. D. Theis and D. G. Schlom, (High Temperature Materials Chemistry IX, edited by K.E. Spear, Vol. 97–39, Electrochemical Society, Pennington, 1997) pp. 610–616.
- ⁶⁴P. Vogt *et al.*, in preparation (2020).
- ⁶⁵P. Mazzolini, A. Falkenstein, C. Wouters, R. Schewski, T. Markurt, Z. Galazka, M. Martin, M. Albrecht, and O. Bierwagen, *APL Mater.* **8**, 011107 (2020).
- ⁶⁶J. Åhman, G. Svensson, and J. Albertsson, *Acta Cryst.* **C52**, 1336 (1996).
- ⁶⁷J. Wei, K. Kim, F. Liu, P. Wang, X. Zheng, Z. Chen, D. Wang, A. Imran, X. Rong, X. Yang, F. Xu, J. Yang, B. Shen, and X. Wang, *J. Semicond.* **40**, 012802 (2019).
- ⁶⁸E. Ahmadi, O. S. Koksaldi, X. Zheng, T. Mates, Y. Oshima, U. K. Mishra, and J. S. Speck, *Appl. Phys. Express* **10**, 071101 (2017).
- ⁶⁹D. G. Schlom and J. S. Harris, *MBE Growth of High Tc Superconductors* (Molecular Beam Epitaxy: Applications to Key Materials, edited by R.F.C. Farrow (Noyes, Park Ridge), 1995) pp. 541–542.
- ⁷⁰P. Vogt *et al.*, in preparation (2020).
- ⁷¹E. Ahmadi, O. S. Koksaldi, S. W. Kaun, Y. Oshima, D. B. Short, U. K. Mishra, and J. S. Speck, *Appl. Phys. Express* **10**, 041102 (2017).
- ⁷²F. V. E. Hensling *et al.*, in preparation (2020).
- ⁷³M. Barone *et al.*, in preparation (2020).
- ⁷⁴T. Zacherle, P. C. Schmidt, and M. Martin, *Phys. Rev. B* **87**, 023206 (2013).
- ⁷⁵J. Park *et al.*, in preparation (2020).
- ⁷⁶Y. E. Suyolcu *et al.*, in preparation (2020).
- ⁷⁷D. G. A. Gamal, A. T. Nagat, M. M. Nassary, and A. M. Abou-Alwafa, *Cryst. Res. Technol.* **31**, 359 (1996).
- ⁷⁸N. Teraguchi, F. Kato, M. Konagai, K. Takahashi, Y. Nakamura, and N. Otsuka, *Appl. Phys. Lett.* **59**, 567 (1991).
- ⁷⁹J. H. Greenberg, V. A. Borjakova, and V. F. Shevelkov, *J. Chem. Thermodyn.* **5**, 233 (1973).
- ⁸⁰T. Okamoto, A. Yamada, and M. Konagai, *J. Cryst. Growth* **175**, 1045 (1997).
- ⁸¹T. D. Golding, P. R. Boyd, M. Martinka, P. M. Amirtharaj, J. H. Dinan, S. B. Qadri, D. R. T. Zahn, and C. R. Whitehouse, *J. Appl. Phys.* **65**, 1936 (1989).
- ⁸²V. P. Bhatt, K. Giresan, and G. R. Pandya, *J. Cryst. Growth* **96**, 649 (1989).